

# Large elements and advanced beamformers for increased field of view in 2-D ultrasound matrix arrays

Mick Gardner, Michael L. Oelze

*Electrical and Computer Engineering, University of Illinois at Urbana-Champaign, 306 N Wright St, Urbana, IL, 61801, USA*

---

## Abstract

Three-dimensional (3D) ultrasound promises various medical applications for abdominal, obstetrics, and cardiovascular imaging. However, ultrasound matrix arrays have extremely high element counts limiting their field of view (FOV). This work seeks to demonstrate an increased field-of-view using a reduced element count array design. The approach is to increase the element size and use advanced beamformers to maintain image quality. The delay and sum (DAS), Null Subtraction Imaging (NSI), directional coherence factor (DCF), and Minimum Variance (MV) beamformers were compared. K-wave simulations of the 3D point-spread functions (PSF) of NSI, DCF, and MV display reduced side lobes and narrowed main lobes compared to DAS. Experiments were conducted using a multiplexed 1024-element matrix array on a Verasonics 256 system. Elements were electronically coupled to imitate a larger pitch and element size. Then, a virtual large aperture was created by using a positioning system to collect data in sections with the matrix array. High-quality images were obtained using a coupling factor of two, doubling the FOV while maintaining the same element count in the virtual large aperture as the original matrix array. The NSI beamformer demonstrated the best resolution performance in simulations and on the large aperture, maintaining the same resolution as uncoupled DAS for coupling factors up to 4. Our results demonstrate how larger matrix arrays could be constructed with larger elements, with resolution maintained by advanced beamformers.

**Keywords:** Beamforming, ultrasound matrix arrays, 3D ultrasound, large elements, null subtraction imaging

---

## 1. Introduction

Three-dimensional (3D) ultrasound is an emerging and attractive technique in the medical imaging community because it can provide full-volume views of a region of interest while being portable, safe, and capable of real-time imaging. Volume imaging with ultrasound has various medical applications in obstetrics, musculoskeletal, and cardiovascular imaging to name a few examples [1]. However, 3D ultrasound imaging usually requires a fully populated 2D matrix array. Such arrays have a prohibitively high number of array elements, e.g. 1024 elements in a 32x32 system. With an array pitch typically around one wavelength or less to prevent grating lobes during beam steering, the field of view (FOV) of such probes can be severely limited. Also, most ultrasound scanners are not equipped with enough input channels to receive data from such a high element count, so multiplexers are often used to switch between sections of the array on different transmit/receive events [2]. However, in this case, frame rates are limited by

the need for multiple transmit/receive events to acquire all aperture data. With a 4x1 multiplexer, anywhere between 4 - 16 transmit events would be needed to acquire, for example, a single plane-wave angle [3].

To handle higher element counts, so called “microbeamformers” have been integrated into the handles of the transducers [4, 5]. With microbeamforming, the delay-and-sum (DAS) operation is partially performed on ASICs inside the transducer handle on patches of elements. Then, only one wire per patch needs to go back to the scanner for the remaining time delay compensation. With this approach, probes have been designed with over 9,000 active elements [6]. However, the micro-beamformers introduce deviations from ideal time delays due to static focusing and quantization [7]. Micro-beamformed patches often have a fixed focal depth to simplify the hardware, which is not always aligned with the dynamic receive focus when beamforming across patches [7]. Delay quantization is also introduced by the micro-beamformer architecture,

which might use a sample-and-hold method that can only delay signals by discrete time intervals determined by an input clock [8]. These quantizations can reduce the resolution and contrast of high-frame rate images, especially for larger micro-beamformed patches [9].

Other approaches allow the FOV to extend beyond the footprint of the array. These approaches include convex and phased arrays [10], as well as panoramas (also called extended field-of-view or EFOV) [11]. With convex and phased arrays, the field of view can extend beyond the probe footprint due to array curvature or beam steering, respectively. However, with this approach, maintaining resolution over the FOV is a challenge because scan lines become more spread out with depth. With panoramas, the field of view is extended by translating the probe to multiple locations, acquiring an image at each location, then applying some image registration method to align the different views [12, 13]. The issue with panoramas is they can only acquire static images, never real-time video data, because of the need to translate the probe to multiple locations.

A few alternative approaches to array design allow for larger footprints, and thus larger FOVs, with a reduced element count. Extensive work has been done to explore sparse arrays as an option for reducing the element count of 2D ultrasound arrays [14]. With sparsity, element spacing is allowed to increase far beyond the usual  $1/2 - 1$  wavelength in some kind of optimized pattern. The most serious drawback of sparse arrays is that they have reduced transmit power and SNR because of the low element count and small elements. Larger elements have been used in sparse, periodic arrays used for ultrasound localization microscopy (ULM) [15, 16, 17]. With very large elements, the directivity of elements raises the minimum F-number of the array, reducing resolution. For ULM, researchers overcame this issue by placing a diverging acoustic lens over each element to widen the directivity [17]. A wider directivity will introduce grating lobes into the point-spread function (PSF) of the imaging system when the array pitch is greater than one wavelength. The lens approach is successful with ULM because ULM displays the tracks of moving microbubbles over many thousands of frames, and the microbubble localization and tracking algorithms are able to ignore grating lobes. However, for B-mode imaging, grating lobes create artifacts that can obscure other image details [18, 19], meaning a lens which allows grating lobes to appear would not be optimal.

Another example of a reduced element count array design is a row-column addressed (RCA) array [20]. These are fully populated arrays where instead of addressing individual elements, entire rows or entire

columns are accessed at once. This effectively creates two orthogonal arrays of long, line elements, reducing the element count from  $N \times N$  to  $N + N$ . However, the main limitation of these arrays are that they cannot focus or steer along diagonals, they can only focus or steer in a cross (rows, then columns, or vice-versa). This means that resolution will be lower with RCA arrays compared to fully addressed arrays which can steer and focus along both directions at once, in both transmit and receive.

The design we propose is a periodic matrix array with large, square elements. Rather than using a lens, we also propose the use of adaptive or non-linear beamformers for the task of regaining resolution lost by increased element directivity. Several beamformers have been studied for their effectiveness at improving resolution and contrast. The Null Subtraction Imaging (NSI) beamformer has been shown to greatly improve resolution in 2D B-mode images [21], and reduce grating lobe artifacts [22, 19]. The NSI beamformer was also recently implemented on a 2D array for 3D imaging [23]. Coherence factor beamformers have often been used for improving contrast, and they can have benefits to resolution as well. Recently, a Directional Coherence Factor (DCF) beamformer was proposed specifically for use in matrix arrays [24], which calculates coherence on directional projections of matrix data, then combines directions for improved resolution. The Minimum Variance (MV) beamformer has also been shown to greatly improve resolution for 1D arrays [25], but has not been extensively used on 2D matrix arrays due to computational complexity. Therefore, we implemented MV on the same directional projections as DCF to reduce the data size [24]. The resolution improvement makes these beamformers attractive for solving the issues one would encounter when creating an array with a larger pitch and element size.

The goals of this paper are to demonstrate how larger elements can lead to larger apertures without increase to element count and to determine which beamformer is best for maintaining resolution with large elements. To test our approach of using large, square elements, we used a commercial matrix array and electronically coupled adjacent elements to act as if they were one element. To demonstrate a larger aperture, we also used a positioning system to acquire data from a virtual aperture where data was collected in quadrants. Images were beamformed with DAS, NSI, DCF, and MV beamformers for quality comparison.

## 2. Background Theory

This section will give a brief analysis on the effects of increased element size on the beam pattern of a 2D matrix array. The array beam pattern is the product of two factors: an array factor arising from element spacing, and an element factor (often referred to as the directivity) arising from element size. Mathematically, this can be expressed as

$$B(\theta) = H(\theta)G(\theta) \quad (1)$$

where  $B(\theta)$  is the beam pattern, while  $H(\theta)$  and  $G(\theta)$  are the array factor and element directivity respectively. The far-field directivity of an element is given by its spatial Fourier transform. A square element can be represented by two orthogonal rectangle functions, as in

$$A(x, y) = \text{rect}\left(\frac{x}{W}\right)\text{rect}\left(\frac{y}{H}\right) \quad (2)$$

where  $A(x, y)$  is the aperture function,  $W$  is the width and  $H$  is the height of the element. Because these two rectangle functions are independent, we can separate the 2D spatial Fourier transform of the aperture into two 1D spatial Fourier transforms along the  $x$ - and  $y$ - axes, leading to

$$\begin{aligned} \mathcal{F}\{A(x, y)\} &= \mathcal{F}_x\left\{\text{rect}\left(\frac{x}{W}\right)\right\} \times \mathcal{F}_y\left\{\text{rect}\left(\frac{y}{H}\right)\right\} \\ &= W\text{sinc}\left(\frac{Wk_x}{2}\right) \times H\text{sinc}\left(\frac{Hk_y}{2}\right) \end{aligned} \quad (3)$$

where  $\mathcal{F}\{\cdot\}$  denotes the spatial Fourier transform, and  $k_x$  and  $k_y$  are the wave numbers in the  $x$  and  $y$  directions. From Equation (3), increased  $W$  and  $H$  values create more narrow sinc functions, representing how larger element are less sensitive to off-axis echoes. This directivity raises the achievable F-number of the array, which is given by [24]:

$$F^\# = \frac{z}{\text{aperture}} = \frac{1}{2 \tan(\alpha)} \quad (4)$$

where  $z$  is imaging depth and  $\alpha$  is the -3 dB angle of the directivity. This raised F-number will reduce the lateral resolution that can be achieved with the array when using DAS beamforming.

Lastly, we are using coupled elements as an approximation of large elements. A block of coupled elements will have gaps, called the kerf, from the saw used to cut the piezo-electric elements. Figures 1a and 1c display representations of a coupled element (with kerf gaps) and a large element (without kerf gaps), while Figures 1b and 1d display the corresponding 2D spatial Fourier

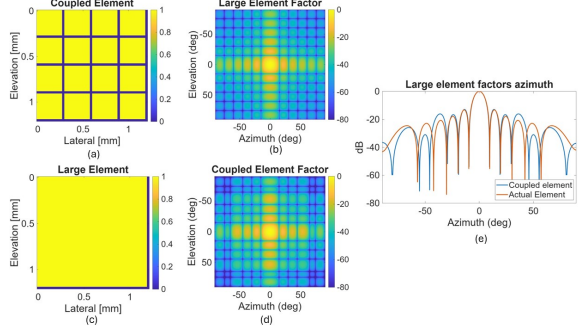


Figure 1: The left column displays representations of (a) a block of coupled elements and (c) and a large element, with corresponding Fourier transforms representing their directivities in (b) and (d). (e) is the cross section of the 2D Fourier transforms at an elevation of 0. Note there are only small differences in the side lobes, meaning coupled elements are a good approximation of a large element, despite kerf gaps.

transforms. Figure 1c displays an azimuthal cross section of both directivities at an elevation angle of zero. From these figures, it can be observed that the kerf gaps only create small differences in the side lobes of the directivities, as well as nearly identical main lobes, suggesting that a coupled element is a close approximation of a large element despite the kerf gaps.

## 3. Methods

### 3.1. Simulations

Simulations were conducted in K-wave [26, 27] to examine the point-spread functions of the different beamformers on a large-element array. The simulated array had 64 elements in an 8 x 8 grid, with a pitch of 1.25 mm in both lateral and elevational directions and an element size of 1.20 mm in both directions. The transmitted frequency was 7.81 MHz with a medium sound speed of 1540 m/s, making the wavelength 197  $\mu$ m. The array parameters then translate to a pitch of 6.7  $\lambda$ , and an element size of 6.5  $\lambda$ , where  $\lambda$  is the wavelength. This element size yields a minimum F-number of 7.07. The plane wave transmission sequence consisted of 13 angles, arranged in a star pattern over azimuth and elevation as displayed in Figure 2.

### 3.2. Virtual Large Aperture

A Vermon 1024-element 8 MHz matrix probe (Vermon S.A., Tours, France) was used to create the virtual aperture. The Vermon probe is made up of four panels of 8x32 elements each. Element coupling on this

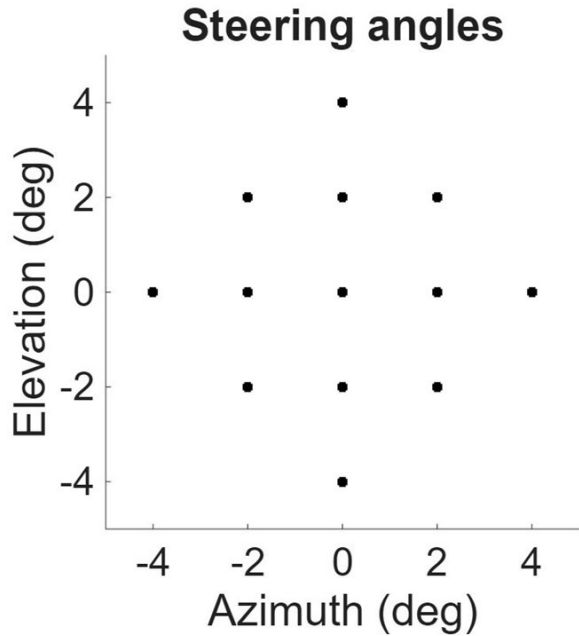


Figure 2: Diagram of transmission angles used for simulations and virtual large aperture experiment. Fewer diagonal angles (i.e. those with both azimuth and elevation components) were included due to increased element width, and thus a narrowed directivity, on the diagonals.

probe was performed by grouping blocks of adjacent elements, averaging their transmission delays, then summing their received channel data. Figure 3 illustrates which elements would be coupled for a coupling factor of 4. Because of the panel separation and multiplexing on the Vermon probe, coupling factors were limited to 1 (i.e. no coupling), 2, and 4 to avoid coupling across panels. Within each block of coupled elements, for a given transmission (e.g. plane-wave angle), the delays would be averaged so that all elements in that block fire at the same time. Then on the receive side, the RF traces from each element in a block would be summed together without applying any time delay. That way received signals superimpose like they would for a single element. By coupling on transmit and receive, each coupled block acted as if it was a single, large element.

To create the virtual large aperture, the probe was attached to a positioning system, and programmed to move into 4 quadrants, as displayed in Figure 4. Transmission delays for 13 plane-wave angles, arranged in a star as displayed in Figure 2, were calculated for each element in the virtual aperture. These angles were chosen based on the directivity of elements with a coupling factor of 4 because the largest elements had the most limited steering capabilities. The width of such

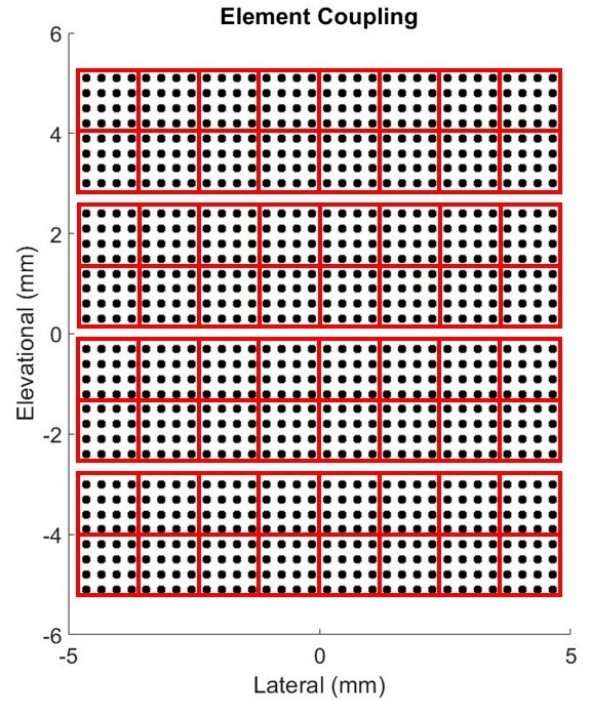


Figure 3: Example of element coupling for a coupling factor of four. Black dots represent the original element positions for the 32 x 32 array. Red boxes represent the larger elements made from coupling. Only coupling factors 1, 2 and 4 were used to divide 32x32 elements evenly and avoid coupling across panels.

elements was  $6.32 \lambda$  in the lateral and elevational directions, leading to a max steering angle of about  $4^\circ$ . Also, these elements were  $6.32\lambda \times \sqrt{2} = 8.98\lambda$  along their diagonals, leading to a max steering angle of about  $3^\circ$  diagonally. Therefore, we chose the star pattern of transmission angles, as opposed to a full square, so that fewer diagonal angles (i.e. those with both azimuth and elevation components) were included. We opted to use the same angle set for all coupling factors for a more direct comparison of quality based only on element size and receive beamforming, even though a larger steering range was available with less coupling.

Once the transmission profiles were calculated, the probe was set in one position, fired the transmission profile associated with the VLA elements in that position, and collected data. Then, the probe was moved to the next position, fired with the corresponding transmission delays, collected data, and so on until the full aperture data was acquired.

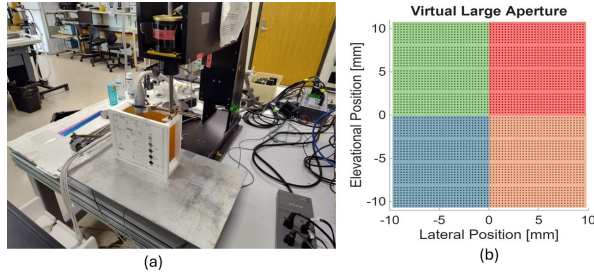


Figure 4: (a) Photograph of the positioning system setup with the general purpose phantom. (b) Diagram of the 4 quadrants making up the virtual large aperture. Each colored square represents one position of the Vermon probe, and its corresponding section of the virtual aperture [21, 22, 19, 29].

### 3.3. Beamforming

#### 3.3.1. Delay-and-Sum

Delay-and-sum (DAS) beamforming is the conventional method of beamforming which simply delays channel data based on transmit and receive distances and sums the delayed data [28]. Received radio-frequency (RF) data were demodulated into In-phase/Quadrature (IQ) data before beamforming. Beamforming was done on a pixel grid with spacing 200  $\mu\text{m}$  in lateral, elevational, and axial directions. Once time delays were applied, transmissions were compounded coherently and elements were summed

$$y(\vec{r}) = \sum_{i=1}^N \sum_{k=1}^M I Q_{i,k}(\tau(\vec{r}, \vec{x}_i)) e^{-j2\pi f_0 \tau(\vec{r}, \vec{x}_i)}. \quad (5)$$

In the above equation,  $y(\vec{r})$  is the beamformed pixel value for pixel  $\vec{r}$ ,  $M$  and  $N$  are the number of transmissions and elements respectively,  $I Q_{i,k}$  is the delayed IQ data from element  $i$  and transmission  $k$ ,  $\tau(\vec{r}, \vec{x}_i)$  is the time delay applied to the IQ data, and  $f_0$  is the center frequency of transmission.

Receive sub-apertures were determined using the minimum constant F-number approach described in [28], where the -3 dB point of the element directivity determined which pixels a given element should contribute to. Elements in the Vermon probe are square, and the lateral width of the elements was used to estimate the directivity and minimum F-number.

#### 3.3.2. Null Subtraction Imaging

Null subtraction imaging is implemented by beamforming with three different apodizations in parallel and incoherently summing the results [21]. These three apodizations are a zero-mean (ZM) apodization, and two direct current (DC) apodizations which are offset

versions of the ZM. The ZM apodization creates a null at 0°, or broadside to the receive sub-aperture. The DC apodizations bridge the null but create similar side lobes in the beam pattern. Once beamforming is done with the three apodizations, the null is subtracted leaving a narrow main lobe and low side lobes [21]. The amount of offset, referred to as the DC offset, is a tunable parameter of NSI typically in the range 0.1-1. In our simulations and experiments, we set the DC offset to 0.5. Lower DC offsets result in more narrow main lobes, more suppressed side lobes, reduced grating lobes, and speckle that is no longer fully developed [21, 22, 19, 29].

To implement NSI on a 2D array, a directional approach was taken as described in [23]. In this approach, two zero-mean apodizations are made by taking an equal number of +1 and -1 along row and column directions of the receive sub-aperture. Once beamforming and envelope detection are done for each ZM apodization, the maximum value over each result is taken as a directional zero-mean, as in

$$E_{ZM} = \max(E_{ZM_{row}}, E_{ZM_{col}}) \quad (6)$$

where  $E$  represents the envelope of a beamformed signal. Beamforming is also performed with two DC offset apodizations for each ZM apodization. For a given ZM apodization, the DC offset apodizations are given by

$$\begin{aligned} DC1_X &= ZM_X + dc \\ DC2_X &= ZM_X - dc \end{aligned} \quad (7)$$

where  $ZM$  represents the ZM apodization,  $dc$  represents the DC offset,  $DC1$  and  $DC2$  represent the DC apodizations, and  $X$  is a placeholder for direction (i.e. row or column). Once beamforming is performed for each DC offset apodization, the envelopes of the beamformed signal in each direction are averaged, as in

$$E_{DC_X} = \frac{E_{DC1_X} + E_{DC2_X}}{2}. \quad (8)$$

Then, a directional DC envelope is taken as the pixel-by-pixel maximum over both directions, same as with the ZM

$$E_{DC} = \max(E_{DC_{row}}, E_{DC_{col}}) \quad (9)$$

Finally, the NSI image is obtained by subtracting the ZM envelope from the DC envelope, as

$$E_{NSI} = |E_{DC} - E_{ZM}| \quad (10)$$

where the absolute value is taken to avoid negative envelope values.

### 3.3.3. Directional Coherence Factor

The Directional Coherence Factor (DCF) involves projecting matrix array data along azimuth and elevational dimensions, calculating a coherence factor for each direction, then multiplying those factors together to get the directional coherence factor [24]. Mathematically, the projected data can be written as

$$\begin{aligned} P_i &= \sum_{j=1}^Q S_{i,j} = [P_1^{AZ}, \dots, P_Q^{AZ}] \\ P_j &= \sum_{i=1}^Q S_{i,j} = [P_1^{EL}, \dots, P_Q^{EL}]^T \end{aligned} \quad (11)$$

where  $P_i$  is the projection onto azimuth,  $P_j$  is the projection onto elevation,  $Q = \sqrt{N}$  is the number of elements in elevation and azimuth, and  $S_{i,j}$  is time-delayed channel data from the element at row  $i$  and column  $j$ . From these projected vectors, a coherence factor is calculated for each of them as

$$\begin{aligned} CF_{AZ} &= \frac{\left| \sum_{i=1}^Q P_i \right|^2}{Q \sum_{i=1}^Q |P_i|^2} \\ CF_{EL} &= \frac{\left| \sum_{j=1}^Q P_j \right|^2}{Q \sum_{j=1}^Q |P_j|^2}. \end{aligned} \quad (12)$$

Finally, the DCF is calculated by multiplying  $CF_{AZ}$  and  $CF_{EL}$ :

$$DCF = CF_{AZ} \times CF_{EL} = \frac{\left| \sum_{i=1}^Q \sum_{j=1}^Q P_i P_j \right|^2}{Q^2 \sum_{i=1}^Q \sum_{j=1}^Q |P_i P_j|^2}. \quad (13)$$

After the DCF value is calculated for each pixel, the pixel is multiplied by the DCF. We note that in the original published method, the authors included diagonal projections [24]. However, for reduced computation, we opted to only include the row and column projections.

### 3.3.4. Minimum Variance

Inspired by the directional projections from DCF, we also performed Minimum Variance (MV) weighting on the projected vectors in Equation 11 [25]. The optimal MV weights are given by

$$\mathbf{w} = \frac{\hat{R}^{-1} \mathbf{a}}{\mathbf{a}^H \hat{R}^{-1} \mathbf{a}} \quad (14)$$

where  $\mathbf{w}$  is the desired weighting vector,  $\hat{R}$  is an estimate of the spatial covariance matrix, and  $\mathbf{a}$  is a steering vector set to all ones. The spatial covariance matrix was

estimated on either direction using spatial smoothing as in

$$\begin{aligned} R_{AZ} &= \frac{1}{Q-L+1} \sum_{l=0}^{Q-L} P_{i,l} P_{i,l}^H \\ R_{EL} &= \frac{1}{Q-L+1} \sum_{l=0}^{Q-L} P_{j,l} P_{j,l}^H \end{aligned} \quad (15)$$

where  $P_{i,l}$  and  $P_{j,l}$  were sub-vectors of the directional projections in Equation 11, defined as the following:

$$\begin{aligned} P_{i,l} &= [P_l^{AZ}, \dots, P_{l+L-1}^{AZ}] \\ P_{j,l} &= [P_l^{EL}, \dots, P_{l+L-1}^{EL}]. \end{aligned} \quad (16)$$

The sub-array size  $L$  was set to  $Q/2$  for both azimuth and elevation projections. In both cases, diagonal loading was also performed on the covariance matrix estimates:

$$\hat{R} = R + \epsilon I \quad (17)$$

where  $I$  is the identity matrix and  $\epsilon = \frac{1}{10L} \cdot \text{trace}\{R\}$  is the diagonal loading factor. After estimating the covariance matrices for either direction, weights were calculated with Equation 14, resulting in a  $\mathbf{w}_{AZ}$  and a  $\mathbf{w}_{EL}$ . Then, projected MV outputs were calculated as

$$\begin{aligned} y_{AZ} &= \frac{1}{Q-L+1} \sum_{l=0}^{Q-L} \mathbf{w}_{AZ}^H P_{i,l} \\ y_{EL} &= \frac{1}{Q-L+1} \sum_{k=0}^{Q-L} \mathbf{w}_{EL}^H P_{j,k} \end{aligned} \quad (18)$$

and finally, directions were combined with

$$y = \sqrt{y_{AZ} y_{EL}^*} \quad (19)$$

where  $y$  is the final directional MV output, and  $*$  denotes complex conjugate.

### 3.3.5. Quality Metrics

To assess the spatial resolution, the full width at half-maximum (FWHM) of the lateral profiles was estimated for images with wire targets. Lateral profiles were taken across the X/Z (lateral/depth slice) of the 3D volumes, averaged axially with depth 0.5 mm and elevationally with width 1 mm. Profiles were then interpolated by a factor of 64 using spline interpolation for FWHM estimates. The contrast of anechoic regions was estimated using the contrast ratio (CR), the contrast-to-noise ratio (CNR) and the generalized contrast-to-noise ratio

(gCNR). These metrics are given by the following equations [30]:

$$CR = 10 \log_{10} \left( \frac{\mu_i}{\mu_o} \right) \quad (20)$$

$$CNR = \frac{\mu_i - \mu_o}{\sqrt{\sigma_i^2 + \sigma_o^2}} \quad (21)$$

$$gCNR = 1 - \int_{-\infty}^{\infty} \min \{ p_i(x), p_o(x) \} dx \quad (22)$$

In the above equations,  $\mu_i$  is the average envelope level inside some region of interest (ROI), and  $\mu_o$  is average envelope level of the background. Likewise,  $\sigma_i^2$  and  $\sigma_o^2$  are the variances of the envelopes in those regions. Finally,  $p_i(x)$  and  $p_o(x)$  are the probability distributions of the envelopes in the same regions. Histograms with 256 bins were used to estimate the distributions.

Finally, to assess speckle quality, the speckle signal-to-noise ratio (sSNR) was also estimated. The sSNR is given by  $sSNR = |\bar{A}| / \sqrt{var(A)}$ , where  $A$  is the envelope level in some region of interest, the value  $\bar{A}$  is the mean and  $var(A)$  is the variance of the envelope in that region [31]. A higher sSNR indicates better speckle quality, with fully developed speckle approaching an sSNR value of 1.91 [31].

## 4. Results

### 4.1. Simulations

Resulting max projections over depth of the simulated point-spread functions are displayed in Figure 5, along with lateral and elevational profiles. Quality metrics are given in Table 1. We observed the highest side lobes with DAS, with main lobe to side lobe contrast of 26.3 dB. The NSI beamformer had the lowest side lobes, with their main lobe to side lobe contrast going down to 41.3 dB. The next lowest side lobes were DCF followed by MV, with contrasts of 30.2 dB and 28.8 dB respectively. In spatial resolution, NSI and DCF achieved similar resolutions in both directions. The NSI and DCF beamformers achieved 1.22 mm and 1.26 mm FWHM estimates respectively in the lateral direction. Then, they achieved 1.25 mm and 1.23 mm in the elevational direction. The MV beamformers demonstrated lowest resolution performance, with FWHM estimates of 1.49 mm and 1.33 mm in lateral and elevational directions respectively. Lastly, DAS displayed the lowest resolution, with FWHM estimates around 2 mm in either direction.

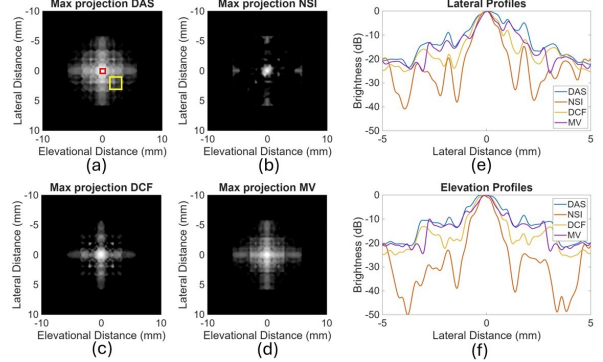


Figure 5: Max depth projection of simulated PSFs of data from an  $8 \times 8$  matrix array with a pitch of 6.7 wavelengths and element size 6.5 wavelengths. (a) DAS, (b) NSI with DC = 0.5, (c) DCF, (d) MV with  $L = Q/2$ . (e) Lateral profile across elevation of 0 mm of each max projection. (f) Elevation profile across lateral position of 0 mm of each max projection. The red and yellow boxes in (a) illustrate the ROIs used for contrast estimates in Table 1. The lateral profiles were used for FWHM estimates.

Beamformer	DAS	NSI	DCF	MV
Lateral	2.29 mm	1.22 mm	1.26 mm	1.49 mm
Elevation	1.81 mm	1.25 mm	1.23 mm	1.33 mm
Contrast	26.3 dB	41.3 dB	30.2 dB	28.8 dB

Table 1: The first two rows are FWHM values along elevation and lateral profiles of simulated PSFs with different beamformers. The last row are contrast estimates of main lobe versus side lobe levels, with ROIs defined in Figure 5a.

### 4.2. Virtual Large Aperture

Table 2 lists coupling factors with corresponding element counts, widths, and F-numbers for the virtual large aperture. With a coupling factor of two, the total element count of the virtual aperture was the same as the Vermon matrix array, meaning the aperture size and FOV have increased by a factor of two in both dimensions with no increase to the element count. Figs. 6-9 display B-mode images acquired with the virtual large aperture. First, Figs. 6-7 display the constant depth slices of wire and cyst phantoms respectively, with each coupling factor and beamformer. Then, Figs. 8-9 display the lateral and elevational slices of the wire and cyst phantoms, again with each coupling factor. Fig. 10 displays lateral profiles for the wire targets and cyst regions. Finally, Fig. 11 displays the charts of quality metrics for each beamformer and coupling factor.

We observed a decrease to resolution with increasing coupling factors, with FWHM estimates going from 0.87 mm with no coupling to 1.88 mm with coupling by four, both with DAS. With a coupling factor of two, FWHM estimates improved from 1.17 mm with DAS to 0.81 mm with NSI beamforming. Overall, the NSI

Coupling Factor	Element Count	Width ( $\lambda$ )	F-number
1	4096	1.48	1.70
2	1024	3.10	3.51
4	256	6.32	7.16

Table 2: Element counts, widths, and minimum F-numbers for each coupling factor on the virtual large aperture.

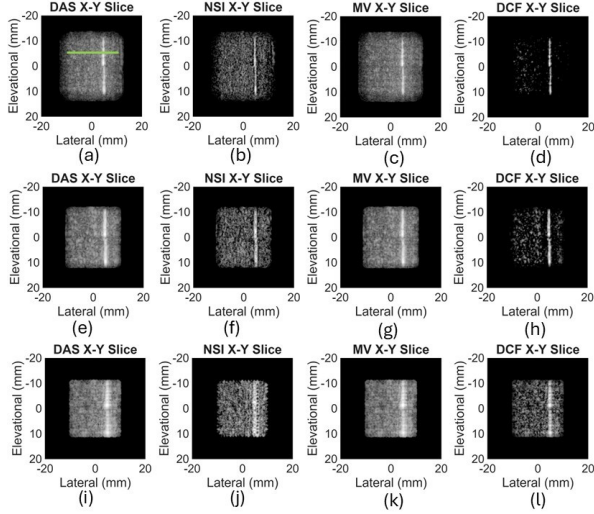


Figure 6: Lateral/elevational slices of the wire phantom from the virtual large aperture. All images are displayed with a dynamic range of 60 dB. (a)-(d) Coupling factor 1 (i.e. no coupling). (e)-(h) Coupling factor 2. (i)-(l) Coupling factor 4. The green line in (a) illustrates the region for the lateral profiles and FWHM estimates.

beamformer performed best for resolution. With contrast metrics, the coupling factors had little effect, while the beamformers influenced the estimates immensely. The DAS beamformer had contrast estimates around -10 dB, CNR estimates near -1, and gCNR estimates near 0.6 for all coupling factors. Overall, DAS performed the best for all contrast metrics and sSNR across all coupling factors. Every other beamformer reduced one or more of the contrast metrics. The DCF beamformer was the worst for CNR (all above -0.6) and sSNR (all below 1), but the best for basic contrast for all coupling factors. The NSI beamformer had the lowest gCNR estimates, consistently around 0.4. The best CNR and gCNR metrics behind DAS came from MV, with those metrics being within 13% of corresponding estimates from DAS across all coupling factors.

## 5. Discussion

Our results demonstrate how larger elements can lead to larger apertures, as well as highlight trade-offs between different beamformers used to maintain resolution.

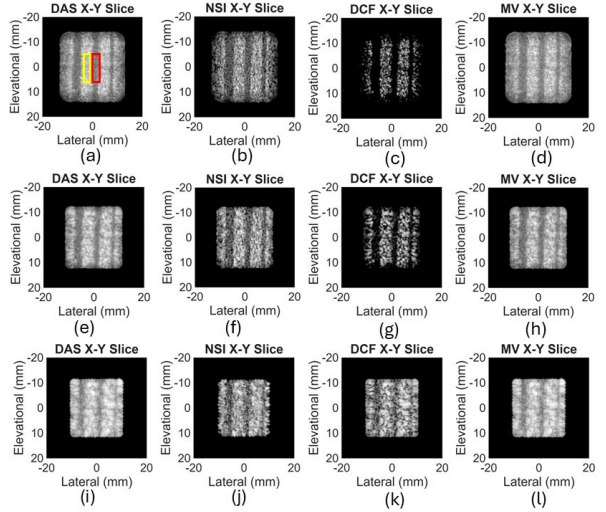


Figure 7: Lateral/elevational slices of the cyst phantom from the virtual large aperture. All images are displayed with a dynamic range of 60 dB. (a)-(d) Coupling factor 1 (i.e. no coupling). (e)-(h) Coupling factor 2. (i)-(l) Coupling factor 4. The red and yellow boxes in (a) illustrate the ROIs for contrast metrics.

tion. We observed that a coupling factor of two on the Vermon array still produced high quality images with advanced beamformers, where the resolution estimates were comparable to resolution estimates of uncoupled DAS. These results provide evidence that matrix arrays with doubled FOV could be produced by doubling the element size, and advanced beamformers can maintain resolution. However, the increased resolution with advanced beamformers also came with a decrease to speckle or contrast metrics. Each of these beamformers has methods of tuning this trade-off, which can help maximize quality for various applications. NSI is tuned by the DC offset [21], DCF could be tuned if performing a GCF calculation on the projections instead of merely CF [24], and MV can be tuned by the diagonal loading factor and sub-array size [25]. Also, a coupling factor of four produced images that were grainy, blurry, and smeared, with a bigger dead zone near the transducer surface, compared to the lower coupling factors. With such a high coupling factor, too few elements are able to contribute to pixel values for any beamforming method to be effective. A coupling factor of four represented an element width of  $6.3 \lambda$ , while a coupling factor of two represented a width of  $3.1 \lambda$  (Table 2). Therefore, the element size cannot be pushed too far above  $3 \lambda$  if using large, square elements in a periodic array.

Comparing the beamformers, we observed that NSI was the best for maintaining resolution compared to DAS, DCF, and MV, based on estimated FWHM val-

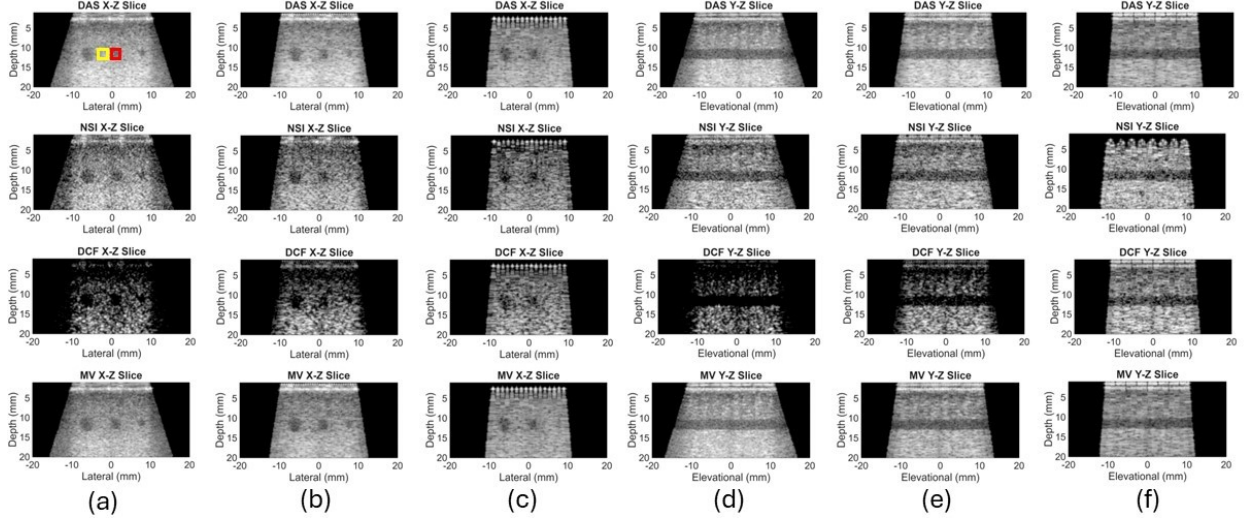


Figure 8: Wire phantom image slices from the virtual large aperture. (a)-(c) Lateral/depth slices. (d)-(f) Elevational/depth slices. (a), (d) Coupling factor 1. (b), (e) Coupling factor 2. (c), (f) Coupling factor 4. Top to bottom: DAS, NSI, DCF, MV beamforming. All images displayed with a 60 dB dynamic range.

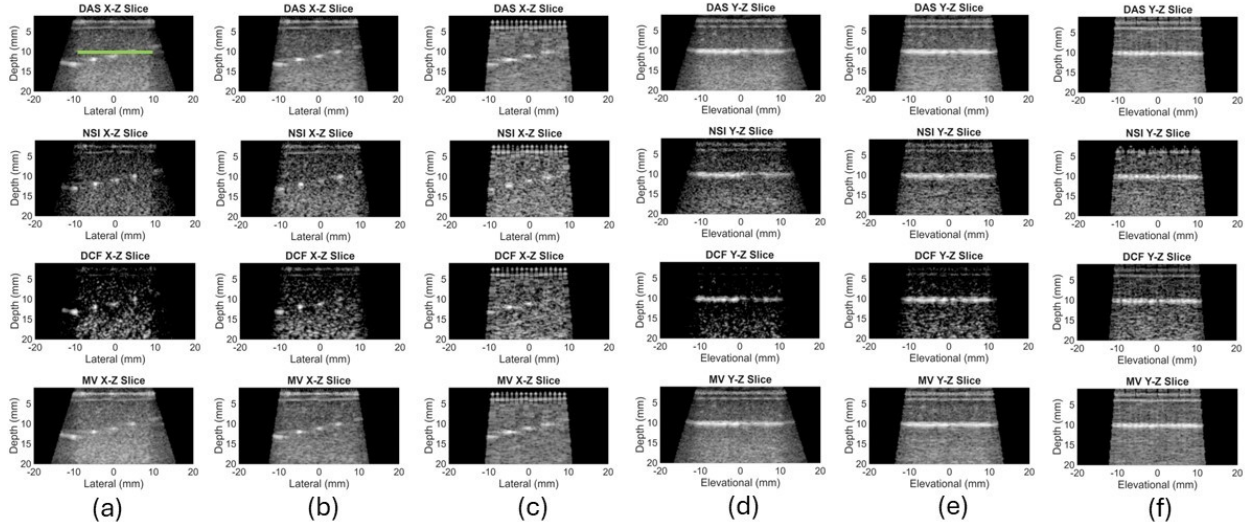


Figure 9: Cyst phantom image slices from the virtual large aperture. (a)-(c) Lateral/depth slices. (d)-(f) Elevational/depth slices. (a), (d) Coupling factor 1. (b), (e) Coupling factor 2. (c), (f) Coupling factor 4. Top to bottom: DAS, NSI, DCF, MV beamforming. All images displayed with a 60 dB dynamic range.

## Lateral Profiles

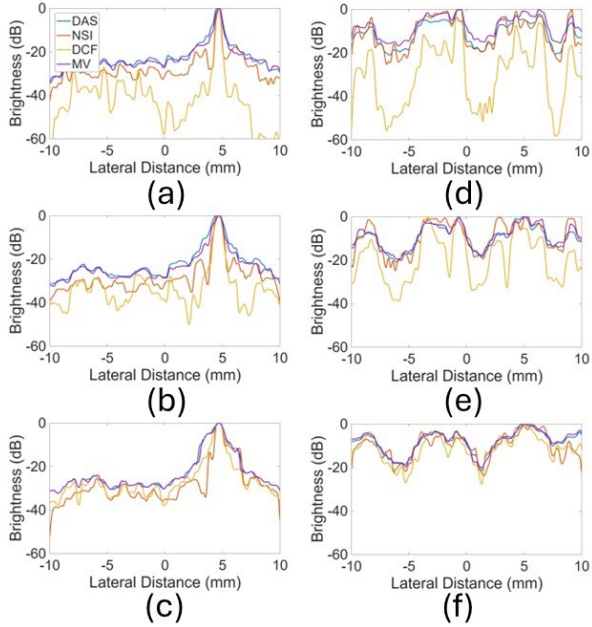


Figure 10: Lateral profiles from the virtual large aperture. (a)-(c) Lateral profiles of a wire target. (d)-(f) Lateral profiles of anechoic regions. (a), (d) Coupling factor 1. (b), (e) Coupling factor 2. (c), (f) Coupling factor 4.

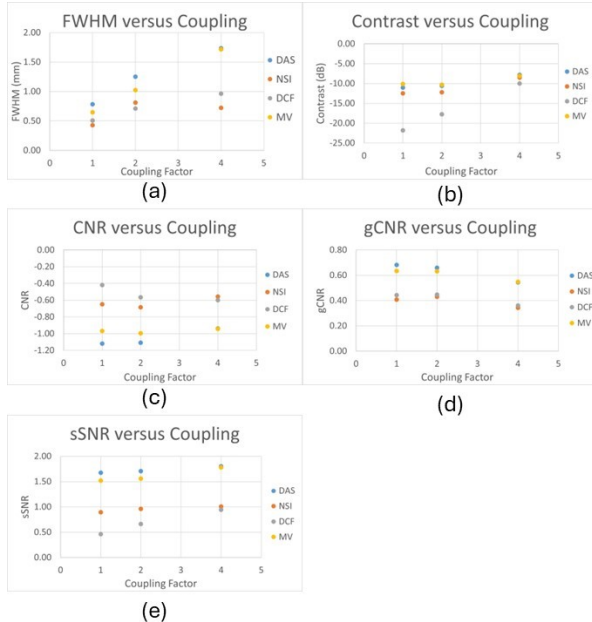


Figure 11: Quality metrics for the virtual aperture. (a) FWHM. (b) Contrast. (c) CNR. (d) gCNR. (e) sSNR.

ues. However, it also reduced the speckle signal significantly, producing the second-lowest sSNR estimates behind DCF. The MV beamformer had the best CNR, gCNR, and sSNR metrics behind DAS for each coupling factor, but it did not improve resolution for coupling factors of two or four, making it the least suitable for large-element array designs. This difference in performance can be explained by considering the fact these beamformers were used in a low-element count scenario. With NSI, the fundamental idea is to form and invert a null [21]. A null can be created using as little as two elements, one positive and one negative, meaning this method should still be effective with fewer elements. However, with MV beamforming, the idea is to calculate apodization weights that minimize the power of the apodized signal while maintaining unit gain at the focal point [25]. With fewer elements, and thus fewer apodization weights, the rejection of signals from outside the focal point is reduced, making MV less effective for low-element count scenarios. The DCF beamformer estimates the coherence of signals across multiple elements, in this case directional projections of the matrix elements. With low element counts, the coherence estimate might be less accurate, making this method less effective with fewer elements as well. It also reduces speckle the most out of all beamformers because speckle signal is not coherent.

Another important consideration for each of these beamformers is the computation that each one requires with respect to the element count. DAS is the most efficient, as it only requires a sum over the elements. In this case, the complexity is  $O(N)$  where  $N$  is the total number of elements. NSI on a 2D array essentially consists of apodizing delayed channel data six times, one for each apodization ( $ZM_{AZ}, ZM_{EL}, DC1_{AZ}, DC1_{EL}, DC2_{AZ}, DC2_{EL}$ ). The remaining operations, such as the extra envelope detections, the DC averaging (Eq. 8), the max over directions (Eqs. 6 and 9), and subtracting the null (Eq. 10) all run in constant time with respect to the elements. Therefore, NSI is also of complexity class  $O(N)$ , with some added constant factors. The DCF beamformer first requires directional projections (Eq. 11), which are sums over rows or columns of channel data. In other words, it sums  $\sqrt{N}$  values  $\sqrt{N}$  times, making the projection calculation  $O(N)$  complexity. The actual coherence factor calculation then only involves summing  $\sqrt{N}$  values from these projected vectors. Therefore, DCF is overall in complexity class  $O(N)$ . Finally, our MV implementation starts with the same projections, then estimates covariance matrices using spatial smoothing on the projections (Eqs. 15 and 16). If the subaperture length for

spatial smoothing is denoted by  $L$ , then  $L \leq \sqrt{N}/2$ , and the size of the covariance matrix is  $L \times L$ . The most computationally expensive operation in MV is then inverting that covariance matrix for the weight calculation (Eq. 14). Inverting an  $L \times L$  matrix is of complexity  $O(L^3)$ . Therefore, our MV implementation has complexity  $O(L^3)$ , or  $O(N^{3/2})$ . Based on the complexities, MV will require the most computation, even for low element counts. To examine the differences between the other three beamformers, we include the run times for coupling factors of two and four with the virtual large aperture in Table 3. From the Table, we observe NSI being the fastest of the advanced beamformers, then DCF, then MV.

Coupling factor	DAS	NSI	DCF	MV
2	86 $\mu$ s	3.1 ms	41 ms	1.42 s
4	91 $\mu$ s	1.2 ms	20 ms	490 ms

Table 3: Run times for different beamformers in low-element count scenarios.

## 6. Conclusion

We have demonstrated in a phantom how a doubled element size (i.e. around  $3 \lambda$ ) can allow for twice the FOV in 2D matrix arrays with no increase to the element count. The resulting loss in resolution from increased element size can be mitigated by advanced beamformers, making large elements more viable. The best beamformer we observed for maintaining resolution was NSI for both simulations and phantom experiments, and it was the most computationally efficient of the advanced beamformers. However, NSI also reduced speckle and contrast metrics. Our approach to array design can allow for larger 2D matrix arrays with an increased FOV with no added electronics. Such an improvement can make 3D ultrasound more viable and useful for clinics without increasing the cost or complexity of 3D ultrasound systems.

## Declaration of Competing Interest

The Authors declare that they have no competing financial interests or personal relationships that appear to have influenced the work reported in this paper.

## Data Availability

Data will be made available upon request.

## Acknowledgments

The authors would like to acknowledge and thank Matt Lowerison and YiRang Shin for performing element calibration on the Vermon matrix array.

This work was supported by the National Institutes of Health [grant numbers R21EB035714, R01CA273700, R01EB036800].

## CRedit Authorship Contribution Statement

**Mick Gardner:** Writing - original draft; Writing - review and editing; Investigation; Formal Analysis; Software. **Michael L. Oelze:** Writing - review and editing; Supervision; Project Administration.

## References

- [1] Q. Huang, Z. Zeng, A Review on Real-Time 3D Ultrasound Imaging Technology, *BioMed Research International* 2017 (2017) 6027029. doi:doi:10.1155/2017/6027029.
- [2] J. Yu, H. Yoon, Y. M. Khalifa, S. Y. Emelianov, Design of a Volumetric Imaging Sequence Using a Vantage-256 Ultrasound Research Platform Multiplexed With a 1024-Element Fully Sampled Matrix Array, *IEEE Transactions on Ultrasonics, Ferroelectrics, and Frequency Control* 67 (2020) 248–257. doi:doi:10.1109/TUFFC.2019.2942557.
- [3] A. Chavignon, B. Heiles, V. Hingot, C. Orset, D. Vivien, O. Couture, 3D Transcranial Ultrasound Localization Microscopy in the Rat Brain With a Multiplexed Matrix Probe, *IEEE Transactions on Biomedical Engineering* 69 (2022) 2132–2142. doi:doi:10.1109/TBME.2021.3137265.
- [4] B. Savord, R. Solomon, Fully sampled matrix transducer for real time 3D ultrasonic imaging, in: *IEEE Symposium on Ultrasonics*, 2003, volume 1, 2003, pp. 945–953 Vol.1. doi:doi:10.1109/ULTSYM.2003.1293556.
- [5] J. M. Rothberg, T. S. Ralston, A. G. Rothberg, J. Martin, J. S. Zahorian, S. A. Alie, N. J. Sanchez, K. Chen, C. Chen, K. Thiele, D. Grosjean, J. Yang, L. Bao, R. Schneider, S. Schaetz, C. Meyer, A. Neben, B. Ryan, J. R. Petrus, J. Lutsky, D. McMahill, G. Corteville, M. R. Hageman, L. Miller, K. G. Fife, Ultrasound-on-chip platform for medical imaging, analysis, and collective intelligence, *Proceedings of the National*

Academy of Sciences 118 (2021) e2019339118. doi:doi:10.1073/pnas.2019339118.

[6] P. Acar, L. Battle, Y. Dulac, M. Peyre, H. Dubourdieu, S. Hascoet, M. Groussolles, C. Vayssi  re, Real-time three-dimensional foetal echocardiography using a new transabdominal xMATRIX array transducer, *Archives of Cardiovascular Diseases* 107 (2014) 4  9. doi:doi:10.1016/j.acvd.2013.10.003.

[7] K.-Q. Zhao, T. G. Bjastad, K. Kristoffersen, Error analysis of subaperture processing in 1-D ultrasound arrays, *IEEE Transactions on Ultrasonics, Ferroelectrics, and Frequency Control* 62 (2015) 663  672. doi:doi:10.1109/TUFFC.2014.006822.

[8] Z. Yu, M. A. Pertijis, G. C. M. Meijer, A programmable analog delay line for Microbeamforming in a transesophageal ultrasound probe, in: 2010 10th IEEE International Conference on Solid-State and Integrated Circuit Technology, 2010, pp. 299  301. doi:doi:10.1109/ICSICT.2010.5667749.

[9] L. Castrignano, P. Tortoli, G. Matrone, M. Crocco, A. S. Savoia, A. Ramalli, On the Impact of Microbeamformers in 3-D High Frame Rate Ultrasound Imaging: A Simulation Study, *IEEE Transactions on Biomedical Engineering* 72 (2025) 1941  1950. doi:doi:10.1109/TBME.2025.3529198.

[10] J. Kang, D. Go, I. Song, Y. Yoo, Wide Field-of-View Ultrafast Curved Array Imaging Using Diverging Waves, *IEEE Transactions on Biomedical Engineering* 67 (2020) 1638  1649. doi:doi:10.1109/TBME.2019.2942164.

[11] S. H. Kim, B. I. Choi, K. W. Kim, K. H. Lee, J. K. Han, Extended Field-of-View Sonography, *Journal of Ultrasound in Medicine* 22 (2003) 385  394. doi:doi:10.7863/jum.2003.22.4.385.

[12] T. C. Poon, R. N. Rohling, Three-dimensional extended field-of-view ultrasound, *Ultrasound in Medicine & Biology* 32 (2006) 357  369. doi:doi:10.1016/j.ultrasmedbio.2005.11.003.

[13] C. Wachinger, W. Wein, N. Navab, Three-Dimensional Ultrasound Mosaicing, in: N. Ayache, S. Ourselin, A. Maeder (Eds.), *Medical Image Computing and Computer-Assisted Intervention – MICCAI 2007*, Springer, Berlin, Heidelberg, 2007, pp. 327  335. doi:doi:10.1007/978-3-540-75759-7\_40.

[14] A. Ramalli, E. Boni, E. Roux, H. Liebgott, P. Tortoli, Design, Implementation, and Medical Applications of 2-D Ultrasound Sparse Arrays, *IEEE Transactions on Ultrasonics, Ferroelectrics, and Frequency Control* 69 (2022) 2739  2755. doi:doi:10.1109/TUFFC.2022.3162419.

[15] H. Favre, M. Pernot, M. Tanter, C. Papadacci, Boosting transducer matrix sensitivity for 3D large field ultrasound localization microscopy using a multi-lens diffracting layer: a simulation study, *Physics in Medicine & Biology* 67 (2022) 085009. doi:doi:10.1088/1361-6560/ac5f72.

[16] H. Favre, M. Pernot, M. Tanter, C. Papadacci, Transcranial 3D ultrasound localization microscopy using a large element matrix array with a multi-lens diffracting layer: an in vitro study, *Physics in Medicine & Biology* 68 (2023) 075003. doi:doi:10.1088/1361-6560/acbde3.

[17] N. Haidour, H. Favre, P. Mateo, J. Reydet, A. Biz  , L. Sambin, J. Dai, P.-M. Chiaroni, B. Ghaleh, M. Pernot, M. Tanter, C. Papadacci, Multi-lens ultrasound arrays enable large scale three-dimensional micro-vascularization characterization over whole organs, *Nature Communications* 16 (2025) 9317. doi:doi:10.1038/s41467-025-64911-z.

[18] Y. Paul, D. Barthez, R. L  veill  , V. Peter, D. Scrivani, Side Lobes and Grating Lobes Artifacts in Ultrasound Imaging, *Veterinary Radiology & Ultrasound* 38 (1997) 387  393. doi:doi:10.1111/j.1740-8261.1997.tb02104.x.

[19] M. Gardner, R. J. Miller, M. L. Oelze, Grating lobe mitigation on large-pitch arrays using null subtraction imaging, *Ultrasonics* 140 (2024) 107302. doi:doi:10.1016/j.ultras.2024.107302.

[20] J. A. Jensen, M. Schou, L. T. J  rgensen, B. G. Tomov, M. B. Stuart, M. S. Traberg, I. Taghavi, S. H.   ygaard, M. L. Ommen, K. Steenberg, E. V. Thomsen, N. S. Panduro, M. B. Nielsen, C. M. S  rensen, Anatomic and Functional Imaging Using Row-Column Arrays, *IEEE Transactions on Ultrasonics, Ferroelectrics, and Frequency Control* 69 (2022) 2722  2738. doi:doi:10.1109/TUFFC.2022.3191391.

[21] A. Agarwal, J. Reeg, A. S. Podkowa, M. L. Oelze, Improving Spatial Resolution Using Incoherent Subtraction of Receive Beams Having Different

Apodizations, *IEEE Transactions on Ultrasonics, Ferroelectrics, and Frequency Control* 66 (2019) 5–17. doi:doi:10.1109/TUFFC.2018.2876285.

[22] Z. Kou, R. J. Miller, M. L. Oelze, Grating Lobe Reduction in Plane-Wave Imaging With Angular Compounding Using Subtraction of Coherent Signals, *IEEE Transactions on Ultrasonics, Ferroelectrics, and Frequency Control* 69 (2022) 3308–3316. doi:doi:10.1109/TUFFC.2022.3217993.

[23] M. Yociss, K. Brown, K. Hoyt, Null Subtraction Beamforming for Improved Vessel Resolution in Volumetric Contrast-Enhanced Ultrasound, in: 2021 IEEE International Ultrasonics Symposium (IUS), 2021, pp. 1–4. doi:doi:10.1109/IUS52206.2021.9593368.

[24] X. Wu, W.-N. Lee, Directional Coherence Factor for Volumetric Ultrasound Imaging with Matrix Arrays, *IEEE Transactions on Ultrasonics, Ferroelectrics, and Frequency Control* (2025) 1–1. doi:doi:10.1109/TUFFC.2025.3557519.

[25] J. F. Synnevag, A. Austeng, S. Holm, Adaptive Beamforming Applied to Medical Ultrasound Imaging, *IEEE Transactions on Ultrasonics, Ferroelectrics, and Frequency Control* 54 (2007) 1606–1613. doi:doi:10.1109/TUFFC.2007.431.

[26] E. Martin, Y. T. Ling, B. E. Treeby, Simulating Focused Ultrasound Transducers Using Discrete Sources on Regular Cartesian Grids, *IEEE Transactions on Ultrasonics, Ferroelectrics, and Frequency Control* 63 (2016) 1535–1542. doi:doi:10.1109/TUFFC.2016.2600862.

[27] B. E. Treeby, J. Budisky, E. S. Wise, J. Jaros, B. T. Cox, Rapid calculation of acoustic fields from arbitrary continuous-wave sources, *The Journal of the Acoustical Society of America* 143 (2018) 529–537. doi:doi:10.1121/1.5021245.

[28] V. Perrot, M. Polichetti, F. Varray, D. Garcia, So you think you can DAS? A viewpoint on delay-and-sum beamforming, *Ultrasonics* 111 (2021) 106309. doi:doi:10.1016/j.ultras.2020.106309.

[29] Z. Kou, M. R. Lowerison, Q. You, Y. Wang, P. Song, M. L. Oelze, High-Resolution Power Doppler Using Null Subtraction Imaging, *IEEE Transactions on Medical Imaging* 43 (2024) 3060–3071. doi:doi:10.1109/TMI.2024.3383768.

[30] A. Rodriguez-Molares, O. M. H. Rindal, J. D’hooge, S.-E. Måsøy, A. Austeng, M. A. Lediju Bell, H. Torp, The Generalized Contrast-to-Noise Ratio: A Formal Definition for Lesion Detectability, *IEEE Transactions on Ultrasonics, Ferroelectrics, and Frequency Control* 67 (2020) 745–759. doi:doi:10.1109/TUFFC.2019.2956855.

[31] R. Wagner, S. Smith, J. Sandrik, H. Lopez, Statistics of Speckle in Ultrasound B-Scans, *IEEE Transactions on Sonics and Ultrasonics* 30 (1983) 156–163. doi:doi:10.1109/T-SU.1983.31404.